photonics

MDPI

Article

All-Dielectric Stochastically Encoded Metasurface for Multifunctional Imaging Across Six-Polarization Channels

Linkun Zhang [1,2], Shangshang Cui [1,2], Mengfei Li [1,2], Xin Cai [1,2], Wenjing Fang [1,2,3,*], Xinye Fan [1,2,3], Xiaowei Yang [1,2,3] and Xueli Geng [1,2,3]

[1] School of Physics Science and Information Technology, Liaocheng University, Liaocheng 252000, China; 18363520952@163.com (L.Z.); cuishang123123@163.com (S.C.); 18663753815@163.com (M.L.); 19861219622@163.com (X.C.); fanxinye@lcu.edu.cn (X.F.); yangxiaowei@lcu.edu.cn (X.Y.); gengxueli@lcu.edu.cn (X.G.)
[2] Shandong Provincial Key Laboratory of Optical Communication Science and Technology, Liaocheng University, Liaocheng 252000, China
[3] The Research Center of System Science, Liaocheng University, Liaocheng 252000, China
* Correspondence: fwj0929@163.com

Abstract

We proposed an all-dielectric stochastically encoded metasurface operating in the 1310 nm near-infrared band, which enables multifunctional optical field manipulation across six independent polarization channels. Utilizing a shared-aperture stochastic matrix-encoding strategy combined with cooperative propagation and geometric-phase decoupling modulation, we investigated stochastically encoded phase distributions, vortex beam profiles, near-diffraction-limited focusing profiles, and the characterization of complex-amplitude multifocal focusing under six independent polarizations. Under left- and right-circularly polarized (LCP/RCP) illumination, vortex beams with topological charges of 1 and 2 have demonstrated substantial enhancement in spatial edge contrast, achieving high edge contrasts of 20 dB and 7.45 dB, respectively, enabling high-fidelity extraction of fine structural boundaries for edge-enhanced imaging. In contrast, near-diffraction-limited focusing under x- and y-polarized illumination has been achieved with numerical apertures (NA) of 0.66 and 0.59, facilitating the realization of bright-field imaging. Significantly, parallel imaging based on complex-amplitude multifocal spot arrays exhibits markedly improved channel isolation, achieving high power ratios of 88.8% and 94.5% under 45° and 135° linearly polarized excitation, respectively. The compact shared-aperture architecture integrates all polarization-controlled functionalities without mechanical tuning, enabling polarization-switchable bright-field imaging, edge detection, and parallel optical manipulation in the near-infrared band.

Keywords: all-dielectric metasurface; stochastically encoded; polarization-switchable imaging; edge-enhanced imaging; bright-field imaging; parallel imaging

Check for updates

Received: 26 June 2026
Revised: 29 July 2026
Accepted: 30 July 2026
Published: 3 August 2026

Copyright: © 2026 by the authors. Licensee MDPI, Basel, Switzerland. This article is an open access article distributed under the terms and conditions of the Creative Commons Attribution (CC BY) license.

1. Introduction

Conventional optical systems possess limited polarization modulation capabilities and support only an extremely small number of polarization channels, falling far short of the growing demand for parallel processing of multidimensional optical fields. Moreover, their cumbersome structural layouts and low functional integration densities result in bulky system volumes and single-functionality. The fundamental contradiction between performance enhancement and device miniaturization has become a critical bottleneck, severely

restricting the practical application and technological advancement of high-precision near-infrared planar optical devices. Therefore, there is an urgent need to develop new strategies that enable compact, multi-channel, multifunctional polarization manipulation [1,2].

Metasurfaces enable precise manipulation of the phase, polarization, and wavefront of light fields through subwavelength structural units, serving as a key technological pathway for developing planar and integrated photonic devices [3–7]. However, existing metasurfaces still exhibit notable shortcomings in terms of the number of polarization channels and functional integration. Most designs support only a few polarization channels, making it difficult to meet the demands of parallel multidimensional optical field manipulation [8,9]. Meanwhile, to achieve functional integration, current approaches commonly rely on partitioned aperture layouts or periodic array configurations. Partitioned aperture designs spatially separate different functional regions, resulting in low effective aperture utilization and scattered optical energy, which hinders the simultaneous realization of high integration density and miniaturization [10]. Periodic structures, on the other hand, are susceptible to grating diffraction effects, generating high-order diffraction components and stray light that lead to severe inter-mode crosstalk [11–13]. Consequently, these architectural deficiencies force an inevitable trade-off among channel capacity, NA, and signal fidelity in existing devices [14–18]. This limitation is evidenced by recent representative designs. While Zheng et al. demonstrated dual-channel complex-amplitude modulation [19] and Zhang et al. achieved single-layer vortex beam edge enhancement [20], their designs remain constrained by limited polarization channels and suboptimal output metrics, such as low amplitude ratios or restricted edge contrasts. Similarly, efforts by Mu et al. utilizing spatial multiplexing [21] and by Li et al. exploring multi-channel polarization mapping [22] frequently compromise on NA or struggle to suppress inter-mode crosstalk effectively. To resolve these fundamental contradictions, our proposed stochastic encoding strategy avoids sub-aperture division. By utilizing a shared-aperture architecture, this approach enables high-fidelity, crosstalk-free multifunctional manipulation across six independent polarization channels without sacrificing integration density, capacity, or numerical aperture.

This work proposed a compact all-dielectric stochastically encoded metasurface at 1310 nm to achieve multifunctional near-infrared imaging across six independent polarization channels. By adjusting the encoding matrix and incident polarization conditions, this design efficiently generates three distinct imaging modalities: vortex beams for edge-enhanced imaging under LCP/RCP excitation, near-diffraction-limited focusing for bright-field imaging under x-/y-polarized illumination, and complex-amplitude multifocal spot arrays for parallel imaging under 45°/135° linearly polarized excitation. The three imaging modalities demonstrate distinct capabilities: under LCP/RCP excitation, vortex beams with topological charges of 1 and 2 deliver edge contrasts of 20 dB and 7.45 dB at focal lengths of 24.91 μm and 35.19 μm, respectively; near-diffraction-limited focusing with x- and y-polarized illumination achieves numerical apertures of 0.66 and 0.59, respectively; complex-amplitude multifocal focusing under 45° and 135° linearly polarized excitation yields power ratios of 88.8% and 94.5% at focal lengths of 65.47 μm and 65.04 μm, respectively. This compact, mechanically tunable-free shared-aperture architecture enhances stability and precise six-channel polarization control, offering a robust platform for polarization-switchable bright-field imaging, edge-enhanced imaging, parallel imaging, and integrated near-infrared photonic applications.

2. Materials and Methods

As conceptually illustrated in Figure 1, the proposed metasurface is designed to achieve independent, multi-plane focusing as an alternative to conventional sub-aperture partitioning [23,24]. By utilizing a unified physical aperture, this approach helps optimize

the effective area for incident polarizations, thereby mitigating the spatial resolution degradation and diffractive artifacts often associated with segmented multi-lens designs [25,26].

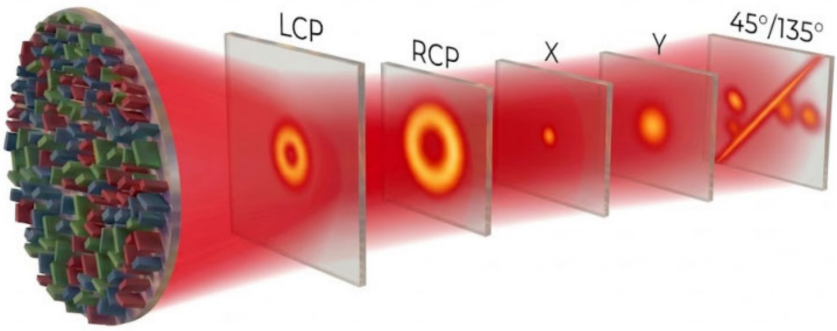


Figure 1. Schematic of the proposed metasurface.

The underlying physical mechanism exploits the high refractive index of silicon (Si) in the near-infrared regime. These high-index nanopillars, arrayed on a highly transparent silica (SiO_2) substrate, are designed to operate as weakly coupled, low-quality-factor resonators via strong local light–matter interactions. This configuration enables efficient phase modulation while preserving high optical transmittance [27–29]. To quantitatively evaluate this optical response, finite-difference time-domain (FDTD) simulations were performed using perfectly matched layer (PML)-absorbing boundaries along the propagation direction (z-axis) and periodic boundary conditions in the transverse plane (x- and y-axes).

The precise geometric design of the meta-atoms is essential to achieve independent control over diverse polarization states [30,31]. Figure 2 illustrates the rectangular nanopillar unit cell utilized for a six-polarization multifunctional modulation stochastic-encoded metasurface, which possesses seven independently tunable parameters $l_x, l_y, l_a, l_b, l_r, l_\theta$, and θ. Through comprehensive parameter scanning and performance optimization, the unit period (P) and nanopillar height (H) were ultimately determined to be 700 nm and 900 nm, respectively, to specifically achieve efficient narrowband operation at 1310 nm for a coherent monochromatic light source. When electromagnetic waves propagate through this structure, each nanocolumn functions as a tunable Jones matrix, whose properties can be customized by altering its lateral dimensions (width W and length L).

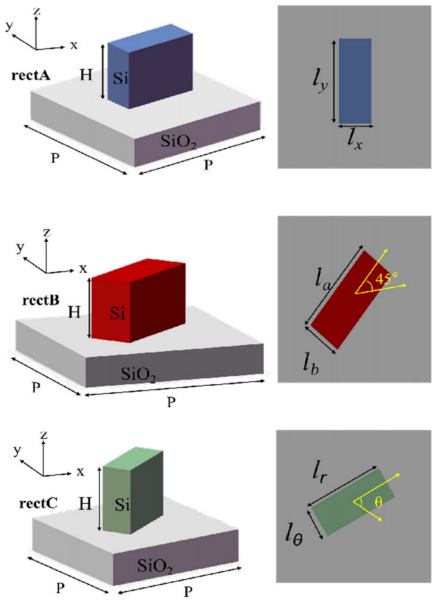


Figure 2. Schematic of the meta-atoms.

As shown in Figure 2, the rect A configuration is designed to modulate both orthogonal x-polarized and y-polarized components simultaneously. The phase shifts (φ_{xx},φ_{yy}) and transmittances (T_{xx},T_{yy}) for the two polarization states are functions of W and L, as depicted in Figure 3. By introducing a 45° in-plane rotation (designated as rect B), the modulation capability is extended to the 45° and 135° linear polarization states as well. For LCP/RCP incidence, rect C adopts a decoupled modulation scheme that combines the propagation phase and geometric phase. The required propagation phase and rotation angle for rect C are governed by Equation (1) [32]:

$$\begin{cases} \varphi_x = (\varphi_{LCP} + \varphi_{RCP})/2 \\ \varphi_y = (\varphi_{LCP} + \varphi_{RCP})/2 - \pi \\ \theta = (\varphi_{LCP} - \varphi_{RCP})/4 \end{cases} \quad (1)$$

where $\varphi_x(\varphi_y)$ denotes the phase response under $x(y)$ polarized incidence, $\varphi_{LCP}(\varphi_{RCP})$ represents the required phase distribution for circularly polarized light, and θ is the rotation angle of the unit cell.

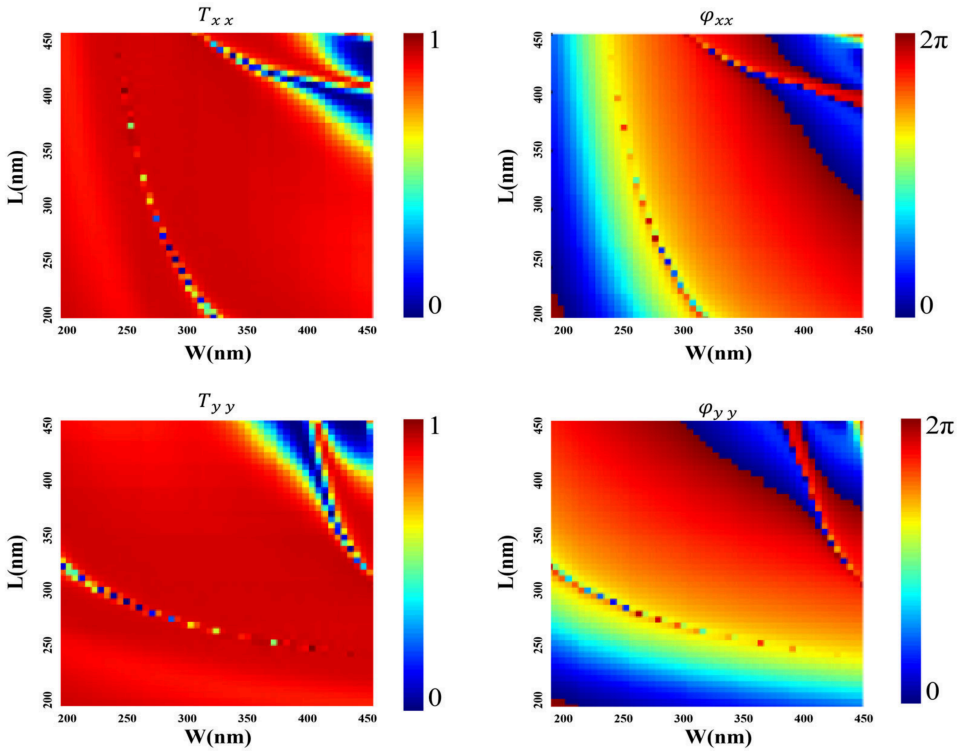


Figure 3. Transmission and phase maps along the x and y directions.

To balance high transmission with full-phase coverage, eight preferred discrete unit structures were selected from the parameter library (as shown in the lookup table in Figure 3). These units exhibit a phase difference of π between their long and short axes, forming a continuous phase gradient ranging from 0 to 2π while maintaining an average transmittance of approximately 90%. Figure 4a shows the transmission and phase relationships of eight unit cells. Based on the encoding sequence, the overall physical structure of the random-encoded metasurface can be constructed by spatially reusing selected meta-atoms from the library within a single shared aperture with a radius of 40 μm, as shown in Figure 4b.

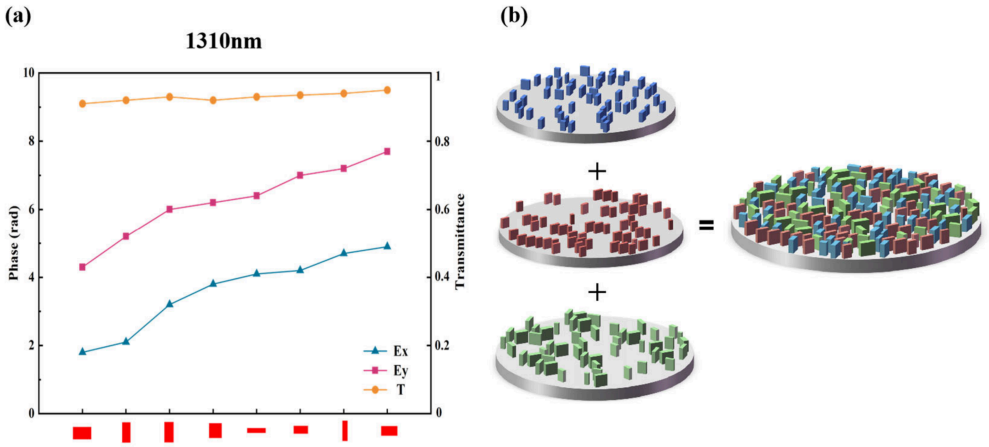


Figure 4. (**a**) Transmission and phase relationship of eight unit cells; (**b**) combined design of the metasurface.

After establishing the phase-unit library, three independent phase distributions were constructed for the metasurface. Firstly, for vortex beams, a focused vortex phase was adopted under LCP/RCP illumination, as described in Equation (2) [33]:

$$\varphi(x_1, y_1) = \frac{2\pi}{\lambda_d}\left(f_g - \sqrt{{x_1}^2 + {y_1}^2 + {f_g}^2}\right) + l\varphi \tag{2}$$

where λ_d = 1310 nm is the design wavelength, f_g is the focal length of the vortex beam under LCP/RCP incidence, l is the topological charge, and φ is the azimuthal angle. Under different incident polarization states, annular intensity distributions with different topological charges are generated at different focal lengths [34].

Secondly, standard spherical-phase profiles were adopted under orthogonal x- and y-linear polarization to realize near-diffraction-limited focusing and high-precision focal spot modulation, which are defined as Equation (3) [35]:

$$\varphi(x_2, y_2) = \frac{2\pi}{\lambda_d}\left(f_i - \sqrt{{x_2}^2 + {y_2}^2 + {f_i}^2}\right) \tag{3}$$

where λ_d = 1310 nm is the design wavelength, and f_i is the focal length of the focal spot under x- or y-polarized incidence.

Thirdly, a complex-amplitude modulation strategy is introduced under 45° and 135° linear polarization to implement multifocal focusing. The target phase distribution and amplitude encoding principle for each focal spot are formulated as follows with Equations (4) and (5) [36]:

$$\begin{cases} \varphi_n(x_3, y_3) = -\frac{2\pi}{\lambda_d}\left(\sqrt{(x_3 - x_{f_n})^2 + (y_3 - y_{f_n})^2 + {z_{fn}}^2} - f_n\right) \\ f_n = \sqrt{{x_{fn}}^2 + {y_{fn}}^2 + {z_{fn}}^2} \end{cases} \tag{4}$$

where φ_n denotes the target phase distribution required to generate a focused beam with focal length f_n; the focal coordinates are $(x_{f_n}, y_{f_n}, z_{f_n})$; and λ_d denotes the design wavelength [37].

$$\begin{cases} E = \alpha_1 \exp(i\varphi_1) + \alpha_2 \exp(i\varphi_2) + \ldots + \alpha_n \exp(i\varphi_n) \\ A = abs(E) \\ \varphi(x_3, y_3) = A \times angle(E) \end{cases} \tag{5}$$

where $\alpha_1 \ldots \alpha_n$ denotes the amplitudes of the focal spots, E is the complex amplitude of the target optical field, A corresponds to its amplitude information, and $\varphi(x_3, y_3)$ is the

amplitude-encoded phase distribution for the multifocal pattern. Based on the above principle, any number of focal spots can be generated at arbitrary positions in the corresponding xy plane under 45° or 135° linearly polarized light, and their intensities can also be controlled.

The aforementioned design involves a total of six phase distributions: φ_X, φ_Y, φ_a, φ_b, φ_{LCP}, and φ_{RCP} (corresponding to x-polarization, y-polarization, 45° polarization, 135° polarization, LCP, and RCP). To achieve crosstalk-free integration within a shared aperture, three stochastic binary matrices M_1, M_2, and M_3 are generated, where the elements "1" account for 33.33% of each matrix and are mutually non-overlapping. These matrices are, respectively, subjected to a Hadamard product: M_1 denotes the biphasic distribution of a vortex beam, M_2 represents the biphasic distribution of near-diffraction-limit focusing, and M_3 indicates the biphasic distribution of complex-amplitude multifocal focusing, yielding the corresponding phase distributions shown in Figure 5. Three key benefits arise from this method. Stray crosstalk among different focusing functions is physically suppressed via stochastic, non-overlapping spatial sampling. Aperture utilization is markedly improved by the parallel recording of dual phases per pixel, enabled by anisotropic polarization decoupling. Meanwhile, higher-order diffraction is effectively mitigated by the statistical uniformity of the random matrices, ensuring high fidelity across all focal planes [38,39].

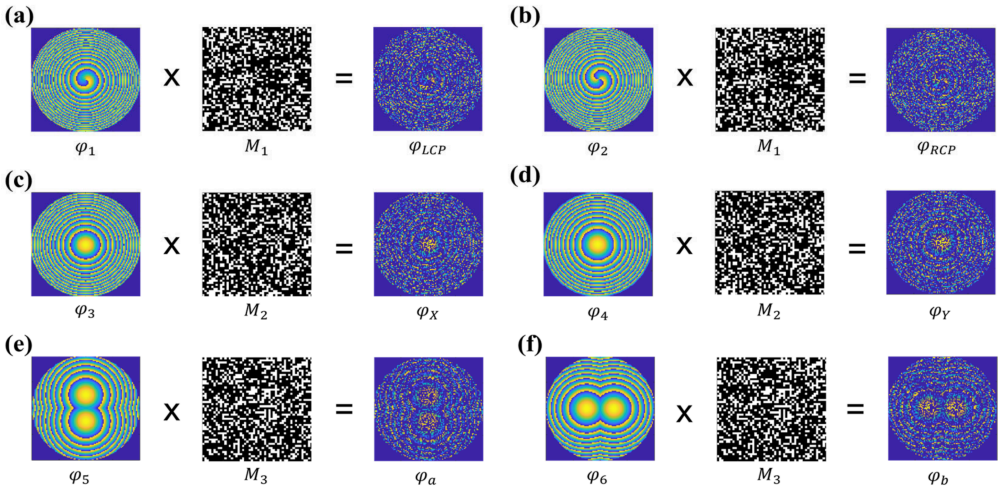


Figure 5. Stochastically encoded phase maps: (**a**) phase distributions under LCP, (**b**) RCP, (**c**) x-polarization, (**d**) y-polarization, (**e**) 45° linear polarization, and (**f**) 135° linear polarization.

Meanwhile, we introduce the spatial autocorrelation index Moran's I (Im). Here, Im ≈ 1 represents highly ordered distributions (e.g., partitioned designing), while Im ≈ 0 denotes completely random layouts. As shown in Figure 6, focus efficiency monotonically increases as the encoding transitions toward complete randomness (Im to 0). Traditional ordered layouts inherently suffer from reduced effective aperture utilization and severe grating diffraction, which concentrate parasitic light into discrete crosstalk peaks. By adopting a stochastic encoding strategy, spatial periodicity is fundamentally broken. Parasitic diffraction energy is thus dispersed into a uniform, negligible background noise floor, allowing more modulated energy to constructively interfere at the focal plane. This validates that random encoding effectively suppresses inter-channel crosstalk, achieving high-fidelity parallel control without sacrificing numerical aperture or integration density [39].

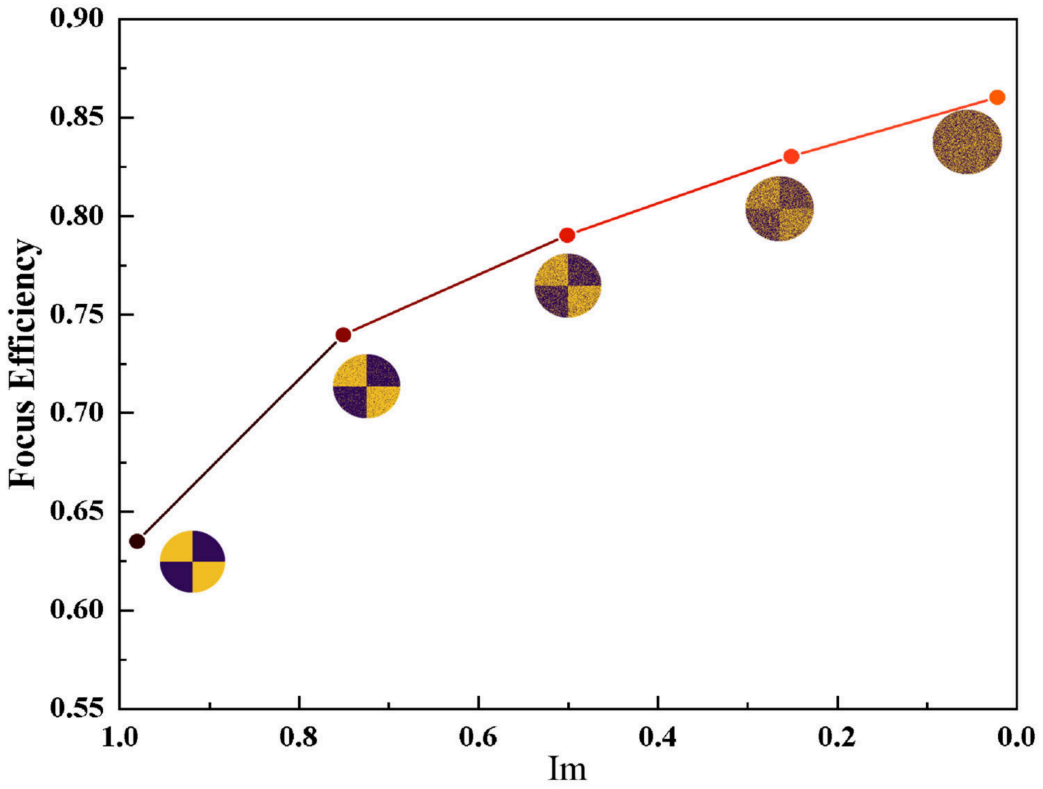


Figure 6. Changes in focus efficiency from ordered to disordered spatial partitioning (functional area ratio of 50%).

3. Results

3.1. Focal Length Characteristics for the Six Polarization States

Based on the design strategy of a shared-aperture stochastic-encoded matrix, we preset specific axial focal lengths for the six independent polarization channels to enable distinct functionalities, including vortex beam generation, near-diffraction-limited focusing, and complex-amplitude multifocal arrays. Simulation results confirm that the achieved focal lengths for all channels are in excellent agreement with the design values. Specifically, for the circular polarization channels used to generate vortex beams, as shown in Figure 7a,b, the designed focal lengths are 25 μm for LCP and 35 μm for RCP, while the simulated focal lengths are 24.91 μm with an error of −0.09 μm and 35.19 μm with an error of +0.19 μm, respectively. For the orthogonal linear polarization channels dedicated to near-diffraction-limited focusing, as depicted in Figure 7c,d, the designed focal lengths are 45 μm for x-polarization and 55 μm for y-polarization, with simulated values of 44.79 μm and 54.89 μm corresponding to errors of −0.21 μm and −0.11 μm, respectively. For the diagonal linear polarization channels used to produce complex-amplitude multifocal arrays, as illustrated in Figure 7e,f, the designed focal length is 65 μm for both 45° and 135° linear polarizations, whereas the simulated focal lengths are 65.47 μm and 65.04 μm with corresponding errors of +0.47 μm and +0.04 μm, respectively. These results demonstrate that the stochastic-encoded shared-aperture design can simultaneously and accurately realize the focal length requirements of multiple polarization channels, with a maximum relative error of less than 0.72%, thereby establishing the physical foundation for the subsequent independent manipulation of each polarization state.

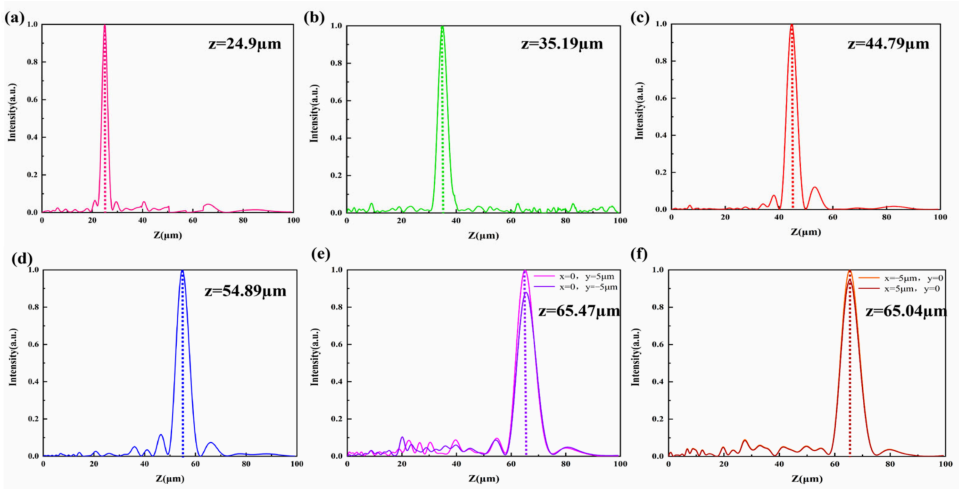


Figure 7. Characterization of focal length performance for the six polarization states: (**a**) simulated focal spot of the vortex beam under LCP illumination at 24.91 μm; (**b**) simulated focal spot of the vortex beam under RCP illumination at 35.19 μm; (**c**) simulated focal spot of the near-diffraction-limited focusing under x-polarized illumination at 44.79 μm; (**d**) simulated focal spot under y-polarized illumination at 54.89 μm; (**e**) simulated multifocal array under 45° linear polarization at 65.47 μm; (**f**) simulated multifocal array under 135° linear polarization at 65.04 μm.

3.2. Vortex Beam Under LCP and RCP Illumination

With the multifunctional random-encoding phase design described above, the proposed metasurface offers polarization-tunable hierarchical focusing modulation. It first functions as a vortex beam, where a standard focusing phase combined with a spiral-phase factor is imparted to the incident wavefront, yielding high-contrast optical field modulation. This phase expression, Equation (6), can be obtained from Equation (2).

$$\begin{cases} \varphi_{LCP}(x_1, y_1) = \frac{2\pi}{\lambda_d}\left(f_1 - \sqrt{{x_1}^2 + {y_1}^2 + {f_1}^2}\right) + l_1\varphi \\ \varphi_{RCP}(x_1, y_1) = \frac{2\pi}{\lambda_d}\left(f_2 - \sqrt{{x_1}^2 + {y_1}^2 + {f_2}^2}\right) + l_2\varphi \end{cases} \quad (6)$$

where λ_d = 1310 nm is the design wavelength; (x_1, y_1) denote the coordinates of the meta-atom structure; the preset focal lengths f_1 and f_2 under LCP and RCP illumination are 25 μm and 35 μm, respectively; and $\varphi_{LCP}(x_1, y_1)$ and $\varphi_{RCP}(x_1, y_1)$ are the required phase distributions under LCP and RCP incidence.

Under LCP illumination, the metasurface imparts a typical spiral-phase gradient, characterized by a continuous 2π azimuthal variation, corresponding to a topological charge of l = 1. Figure 8a presents a side-by-side comparison: the theoretical helical-phase distribution is shown on the left, while the actual stochastically encoded phase pattern following shared-aperture multiplexing is illustrated on the right. It is this multiplexed stochastic phase that physically dictates the structural arrangement on the metasurface. As a result of this modulation, the transmitted optical field carries a unit orbital angular momentum, which gives rise to an annular focal region wherein the central intensity tends to zero. Specifically, at the focal plane of z = 24.91 μm, the intensity distribution exhibits a clear annular profile, where uniform peak intensity surrounds a central dark region with a radius of 0.55 μm, as shown in Figure 8b. This annular focal geometry serves as a spatial filtering kernel, enabling isotropic edge enhancement of input images. Figure 8c demonstrates that the quantitative evaluation of the radial intensity distribution curve indicates a ring width of 0.63 μm. The edge contrast (defined as the ratio of peak ring intensity to the central minimum value) exceeds 20 dB.

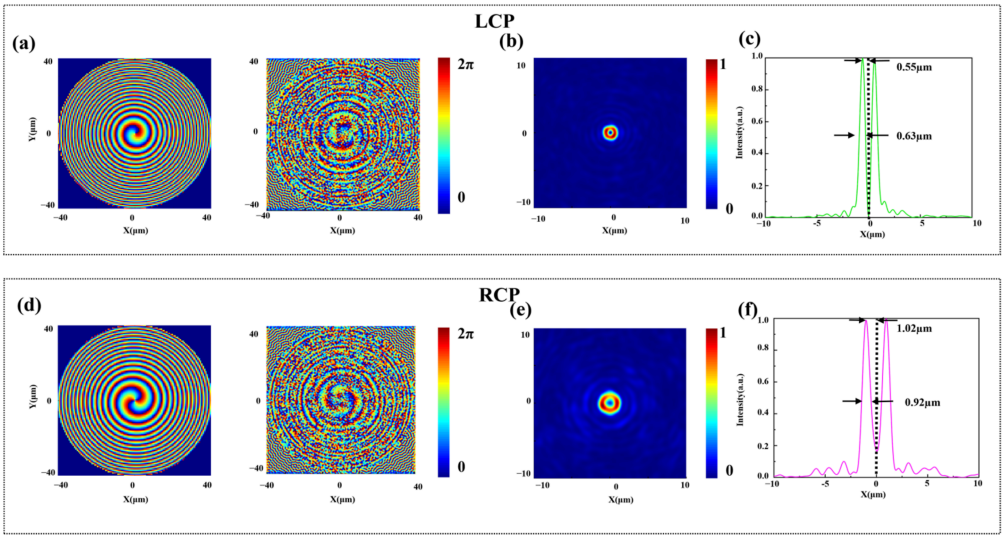


Figure 8. Characterization of vortex beam: (**a**) helical-phase distribution of the metasurface before random encoding at the LCP incidence angle (l = 1) (**left**) and after random encoding with shared aperture (**right**); (**b**) xy-plane intensity distribution of the vortex beam at z = 24.91 μm; (**c**) x-direction intensity distribution of the l = 1; (**d**) helical-phase distribution of the metasurface before random encoding at the RCP incidence angle (l = 2) (**left**) and after random encoding with shared aperture (**right**); (**e**) xy-plane intensity distribution of the vortex beam at z = 35.19 μm; (**f**) x-direction intensity distribution of the l = 2.

Upon switching to RCP incidence, the topological charge becomes l = 2. Similarly, the ideal spiral gradient spanning two complete cycles and its corresponding stochastically multiplexed phase pattern are explicitly depicted in the left and right panels of Figure 8d, respectively. With the higher topological charge, the beam acquires greater orbital angular momentum, causing the optical field to spread radially outward. Consequently, the central dark region expands to a radius of 1.02 μm, as demonstrated in Figure 8e, while the focal position simultaneously shifts axially to z = 35.19 μm. The radial intensity profile in Figure 8f further quantifies this behavior, showing an annular ring width of 0.92 μm while the edge contrast remains above 7.45 dB. These results demonstrate that the higher topological charge yields a broader annular dark core and reduced edge contrast, indicating a tunable spatial filtering response that can be tailored for different edge enhancement requirements.

3.3. Near-Diffraction-Limited Focusing Under x- and y-Polarization Illumination

Secondly, it also possesses the functionality of the near-diffraction-limited focusing mode. The phase distribution required for achieving ideal spherical wave focusing is given by Equation (7).

$$\begin{cases} \varphi_x(x_2, y_2) = \frac{2\pi}{\lambda_d}\left(f_3 - \sqrt{{x_2}^2 + {y_2}^2 + {f_3}^2}\right) \\ \varphi_y(x_2, y_2) = \frac{2\pi}{\lambda_d}\left(f_4 - \sqrt{{x_2}^2 + {y_2}^2 + {f_4}^2}\right) \end{cases} \tag{7}$$

where λ_d = 1310 nm is the design wavelength; $(x_2,\ y_2)$ denote the coordinates of the meta-atom structure; the preset focal lengths f_3 and f_4 under x- and y-polarized illumination are 45 μm and 55 μm, respectively; and $\varphi_x(x_2, y_2)$ and $\varphi_y(x_2, y_2)$ are the required phase distributions under x- and y-polarized incidence.

Figure 9a details the phase modulation mechanism under x-polarized incidence by illustrating the theoretical spherical focusing phase distribution (left) alongside the actual stochastically encoded phase pattern after shared-aperture multiplexing (right). Driven by this multiplexed phase mask, Figure 9b presents the corresponding xy-plane intensity

distribution of the focused spot at z = 44.79 μm. It is clearly evident that even after stochastic multiplexing, the near-diffraction-limited focusing maintains a high energy concentration and extremely low background noise. Meanwhile, its lateral intensity distribution is shown in Figure 9c. The calculated numerical aperture is NA = 0.66, and the measured full width at half maximum (FWHM) is 1.16 μm, which is in excellent agreement with the theoretical diffraction limit, thereby confirming its high-performance near-diffraction-limited focusing characteristics.

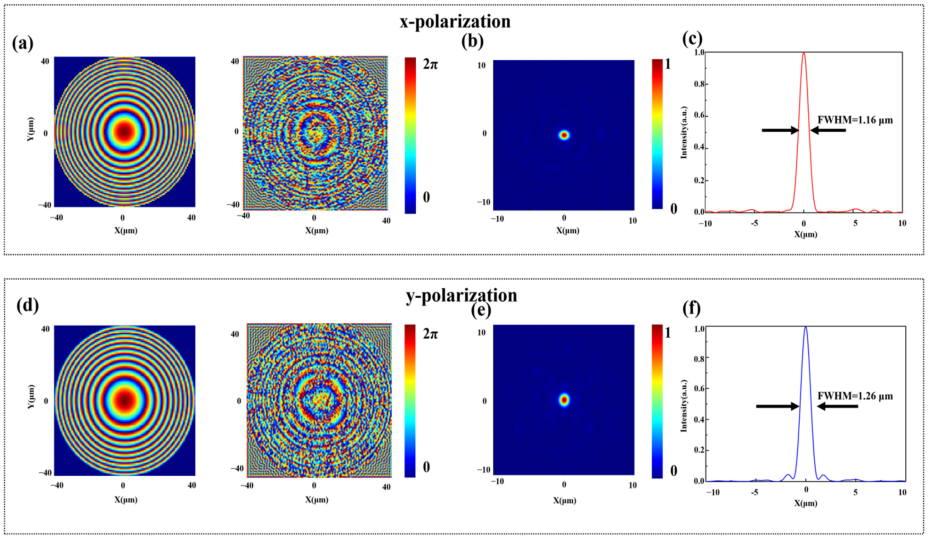


Figure 9. Characterization of near-diffraction-limited focusing: (**a**) helical-phase distribution of a metasurface before random encoding under x-polarized incident light (**left**) and after random encoding with shared apertures (**right**); (**b**) xy-plane intensity distribution of the focused spot at z = 44.79 μm; (**c**) x-direction intensity distribution of the spot at z = 44.79 μm; (**d**) helical-phase distribution of a metasurface before random encoding under y-polarized incident light (**left**) and after random encoding with shared apertures (**right**); (**e**) xy-plane intensity distribution of the focused spot at z = 54.89 μm; (**f**) x-direction intensity distribution of the spot at z = 54.89 μm.

Accordingly, Figure 9d displays the ideal and multiplexed randomly encoded phase distributions under y-polarized incidence, with the corresponding high-quality focal spot at z = 54.89 μm, shown in Figure 9e. The lateral intensity distribution is presented in Figure 9f, where NA = 0.59 with a measured FWHM of 1.26 μm, obtained by calculation, which agrees well with the theoretical diffraction limit. This metasurface structure achieves high-quality, near-diffraction-limited focusing on different axial depths (44.79 μm and 54.89 μm) with no crosstalk between the two channels, providing a solid foundation for bright-field imaging.

3.4. Complex-Amplitude Multifocal Focusing Under 45° and 135° Polarization Illumination

Aside from the above functions, the complex-amplitude multifocal focusing mode can be realized based on independent multifocal phase distributions for the 45° and 135° orthogonal polarization states. The required encoded phase profiles are given by Equation (8) for the 45° polarization state and Equation (9) for the 135° polarization state.

$$\begin{cases} \varphi_1(x_3, y_3) = -\frac{2\pi}{\lambda_d}\left(\sqrt{{x_3}^2 + (y_3 - \xi)^2 + z^2} - f_5\right) \\ \varphi_2(x_3, y_3) = -\frac{2\pi}{\lambda_d}\left(\sqrt{{x_3}^2 + (y_3 + \xi)^2 + z^2} - f_5\right) \\ E_1 = \alpha_1 \exp(i\varphi_1(x, y)) + \alpha_2 \exp(i\varphi_2(x, y)) \\ A_1 = abs(E_1) \\ \varphi_a = abs(E_1) \times angle(E_1) \end{cases} \quad (8)$$

$$\begin{cases} \varphi_3(x_3, y_3) = -\frac{2\pi}{\lambda}(\sqrt{(x_3-\sigma)^2 + {y_3}^2 + z^2} - f_5) \\ \varphi_4(x_3, y_3) = -\frac{2\pi}{\lambda}(\sqrt{(x_3+\sigma)^2 + {y_3}^2 + z^2} - f_5) \\ E_2 = \alpha_1 \exp(i\varphi_3(x,y)) + \alpha_2 \exp(i\varphi_4(x,y)) \\ A_2 = abs(E_2) \\ \varphi_b = abs(E_2) \times angle(E_2) \end{cases} \quad (9)$$

In both equations, the design wavelength is λ_d = 1310 nm, (x_3, y_3) denote the coordinates of the meta-atom structure, f_5 = 65 μm is the preset focal length; z is the axial coordinate of the focal plane, and ξ (or σ) denotes the lateral spatial offset of the sub-focal spots along the corresponding axis. The basic phase distributions $\varphi_1(x_3, y_3)$, $\varphi_2(x_3, y_3)$, $\varphi_3(x_3, y_3)$, and $\varphi_4(x_3, y_3)$ generate two independent focused beams with amplitude-weighting coefficients α_1 and α_2, respectively. E_1 and E_2 are the superposed complex amplitudes of the target optical field, A_1 and A_2 correspond to its amplitude information, and φ_a and φ_b are the final target-encoded phase distributions required for the 45° and 135° polarization states.

Under 45° linearly polarized illumination, to clearly demonstrate the complex-amplitude encoding process, Figure 10a illustrates both the ideal multifocal phase profile (left) and the realistic stochastically encoded phase pattern following shared-aperture multiplexing (right). Its regular gradient enables high-precision modulation, producing multiple clear focal spots at the preset focal plane (z = 65.47 μm), as directly verified by the simulated optical field in Figure 10b. These sub-spots are spaced by about 10 μm along the y-direction with extremely low crosstalk. The longitudinal intensity distribution shown in Figure 10c gives a power ratio of 88.8% for a sub-focal spot.

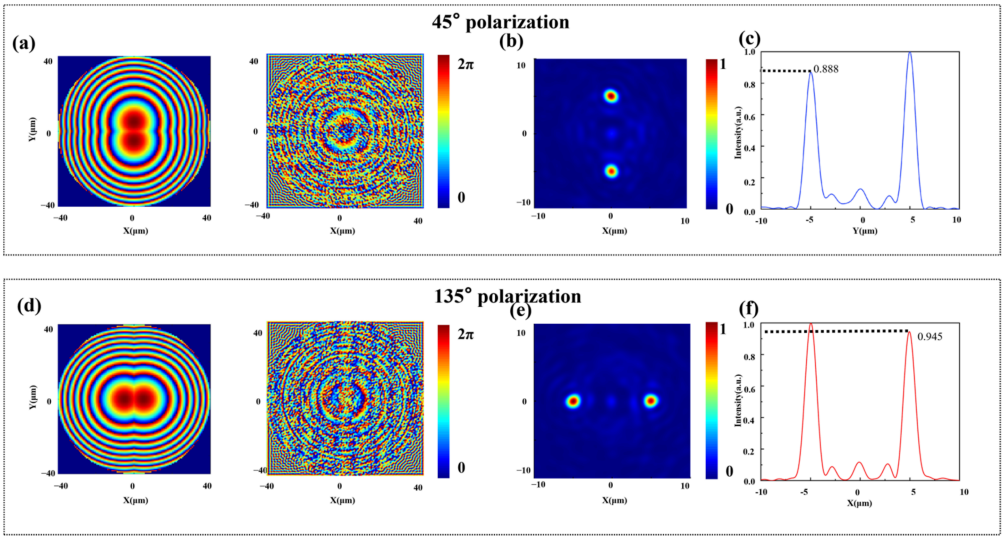


Figure 10. Characterization of complex-amplitude multifocal focusing: (**a**) helical-phase distribution of the metasurface before random encoding under 45° polarized incident light (**left**) and after random encoding with shared aperture (**right**); (**b**) multifocal distribution in the xy plane at z = 65.47 μm under the 45° polarization state; (**c**) longitudinal intensity distribution of the multifocal pattern under the 45° polarization state; (**d**) helical-phase distribution of the metasurface before random encoding under 135° polarized incident light (**left**) and after random encoding with shared aperture (**right**); (**e**) multifocal distribution in the xy plane at z = 65.04 μm under the 135° polarization state; (**f**) lateral intensity distribution of the multifocal pattern under the 135° polarization state.

When the incident polarization is switched to 135°, the independently designed ideal phase profile and its stochastically multiplexed counterpart are as shown in Figure 10d. Governed by this multiplexed pattern, the metasurface generates an equally regular mul-

tifocal pattern at the same axial depth (z = 65.04 μm), but the spots are rearranged along the x-direction with a spacing of 10 μm and a spatial shift, avoiding mutual interference as revealed in Figure 10e. The lateral intensity distribution displayed in Figure 10f yields a power ratio of 94.5%, demonstrating the same excellent focusing stability as in the 45° case.

In summary, the metasurface produces orthogonally arranged and reconfigurable multifocal spots under 45° and 135° linear polarizations, with power ratios of 88.8% and 94.5%, respectively, providing a solid foundation for high-performance parallel imaging.

3.5. Polarization-Controlled Multifunctional Imaging Applications

Modulation transfer function (MTF) analysis, as shown in Figure 11, quantitatively evaluates the six polarization channels and verifies their underlying imaging mechanisms. For bright-field imaging (x- and y-polarization), the MTF curves closely track the theoretical diffraction limits, confirming that the standard spherical-phase design provides high-fidelity near-diffraction-limited focusing by effectively suppressing aberrations. Parallel multifocal imaging channels (45° and 135°) show expected MTF attenuation compared to the bright-field mode, as energy is divided among multiple foci and the longer focal length (65 μm) reduces the effective numerical aperture, lowering high-frequency transmission. Finally, for edge-enhanced imaging (LCP and RCP), a rapid exponential low- to mid-frequency roll-off reflects the vortex beams' spatial high-pass filtering, where the central-phase singularity suppresses low-frequency background contrast. Notably, the RCP channel (topological charge l = 2) exhibits a steeper roll-off than the LCP channel (l = 1) due to its larger central dark core, which yields stronger low-frequency suppression.

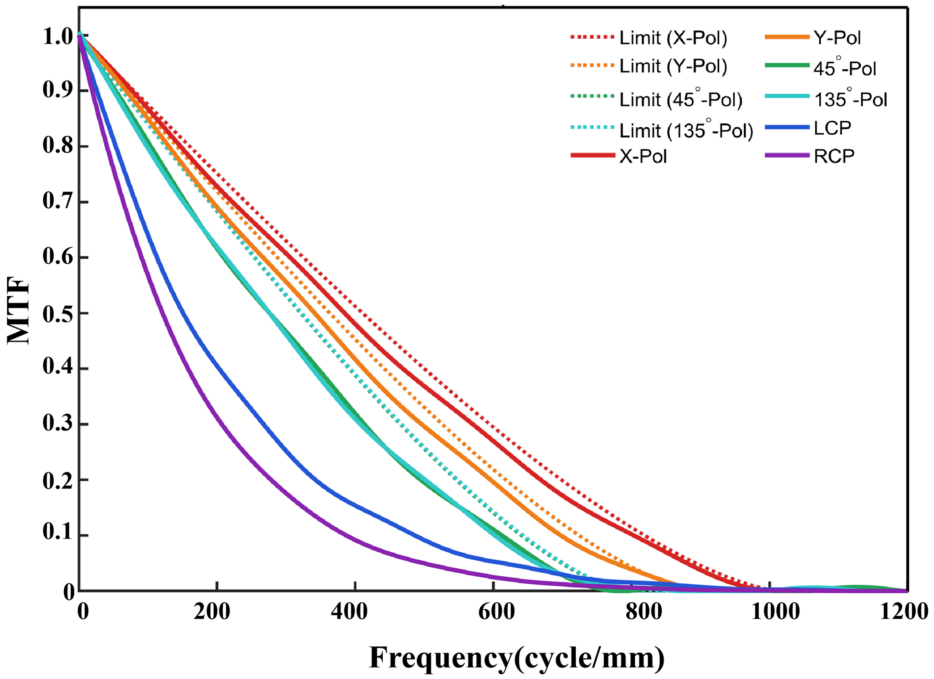


Figure 11. MTF curves of the metasurface for the six polarization states, compared with the theoretical diffraction limits.

To further demonstrate practical application potential in multidimensional optical information processing, we simulated polarization-multiplexed imaging using a standard target symbol "@" at 1310 nm. This symbol contains richer spatial frequency components than simple letters, providing a more rigorous test of imaging fidelity. In all simulations, the incident light is an ideal plane wave at normal incidence, providing uniform amplitude and a strictly defined polarization state. This standard approach extracts the metasurface's

intrinsic phase modulation and polarization conversion capabilities while avoiding interference from spatial fluctuations or wavefront distortions in the incident beam. The electric field of a coherent image is the convolution of the target object's intensity distribution O(x, y) with the system's point-spread function (PSF), as given by Equation (10) [40]:

$$I_i(x, y) = O(x, y) \otimes PSF \tag{10}$$

Here, (x, y) represents coordinates in the image plane, and $I_i(x, y)$ corresponds to the image distribution.

Under circular polarization, the metasurface enables edge-enhanced imaging. With LCP incidence, the spiral-phase gradient acts as a spatial high-pass filter, attenuating low spatial frequencies while retaining high-frequency edges, producing a sharp, high-contrast isotropic edge image of "@", as presented in Figure 12a. With RCP incidence, the larger central dark core of the second-order vortex beam intensifies the filtering effect, resulting in a broader extracted edge contour, as clearly observable in Figure 12b.

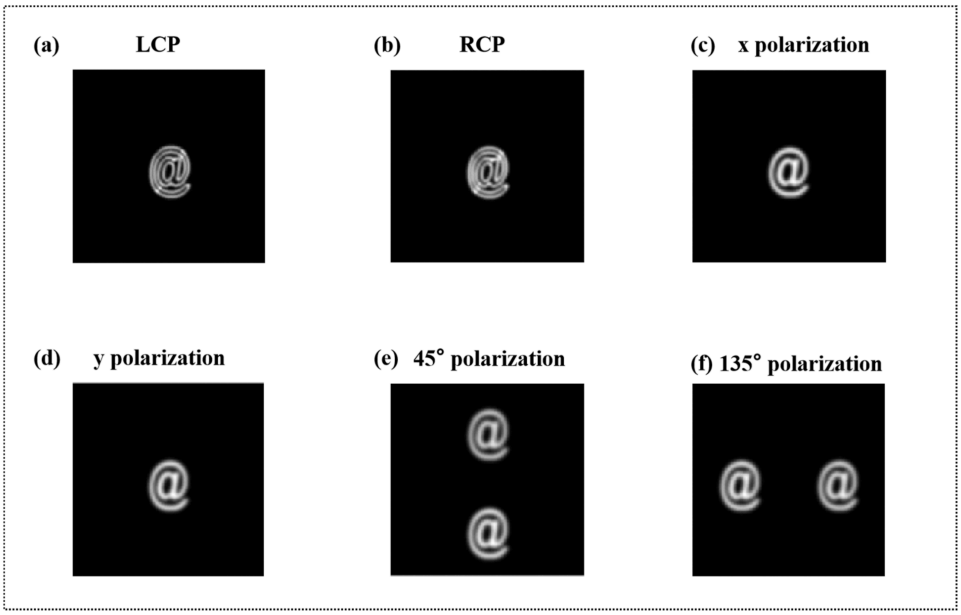


Figure 12. (**a**,**b**) show edge-enhanced imaging; (**c**,**d**) show bright-field imaging; (**e**,**f**) show parallel imaging.

Under orthogonal linear polarizations, the metasurface reverts to near-diffraction-limited focusing for bright-field imaging. Both polarization states yield aberration-free reconstructions of "@", as shown in Figure 12c,d, confirming accurate detail reproduction as a conventional single-focus lens.

Under 45° and 135° linear polarizations, complex-amplitude encoding redistributes incident energy for multi-target replicated imaging. The "@" splits into two vertically separated images under 45° polarization and two horizontally separated images under 135° polarization, as shown in Figure 12e,f. The observed diffraction-induced blurring is consistent with the energy dispersion inherent to multifocal modulation, and the MTF curves in Figure 11 quantitatively capture this expected trade-off.

4. Discussion

Through a performance comparison with recent representative state-of-the-art designs, as summarized in Table 1, the proposed design demonstrates competitive performance across all three imaging modalities. For edge-enhanced imaging via vortex beam genera-

tion, spatial edge contrasts of 20 dB and 7.45 dB are achieved in the LCP and RCP channels, respectively, which compare favorably with previously reported single-layer architectures and spin-multiplexed designs [20,41]. For bright-field imaging under orthogonal linear polarizations, the device maintains near-diffraction-limited focusing with numerical apertures of 0.66 and 0.59, respectively. Existing high-NA designs [42,43], though exhibiting excellent focusing performance, remain functionally limited, while some previous works [22,39] that achieved six-polarization-channel coverage have, likewise, been confined to a single focusing function. For parallel imaging, power ratios of 88.8% and 94.5% are obtained under 45° and 135° linearly polarized excitation, respectively, which are improved over the values reported for conventional spatial multiplexing schemes [19,21]. These results suggest that, by virtue of the stochastic encoding strategy, the present design is able to support edge-enhanced imaging, bright-field imaging, and parallel imaging simultaneously within a single shared aperture, while effectively suppressing inter-channel crosstalk, thereby offering a viable technological pathway toward high-performance multifunctional integrated metasurfaces.

Table 1. Comparison of the proposed metasurface with representative prior works. (× = feature not available, √ = feature available).

Author	Channel Counts	Vortex Beam	Focusing	Multifocal	NA	Edge Contrast	Power Ratio
Z et al. [19]	2	×	×	√	N/A	N/A	44.4%
Zhang et al. [20]	1	√	×	×	N/A	7.6 dB	N/A
Mu et al. [21]	2	×	×	√	N/A	N/A	66.6%
Li et al. [22]	6	×	√	×	N/A	N/A	N/A
Li et al. [39]	6	×	√	×	N/A	N/A	N/A
Yao et al. [41]	2	√	√	×	N/A	N/A	N/A
Wu et al. [42]	2	×	√	×	0.7	N/A	N/A
Khalilian et al. [43]	1	×	√	×	0.95	N/A	N/A
This work	6	√	√	√	0.66	20 dB	94.5%

5. Conclusions

We have demonstrated a six-polarization multifunctional all-dielectric stochastically encoded metasurface operating at 1310 nm, which exploits a shared-aperture random matrix-encoding strategy combined with decoupled propagation and geometric-phase modulation to enable multifunctional near-infrared imaging across six polarization channels within a single monolithic platform. The stochastic encoding approach physically suppresses inter-mode crosstalk and higher-order diffraction via non-overlapping spatial sampling while maximizing aperture utilization through dual-phase recording per pixel, thereby allowing the device to concurrently support three distinct imaging modalities: edge-enhanced imaging via vortex beams (topological charges l = 1 and 2 with edge contrasts >20 dB and 7.45 dB), bright-field imaging via near-diffraction-limited focusing (NA of 0.66 and 0.59), and parallel imaging via complex-amplitude multifocal arrays (power ratios of 88.8% and 94.5%) under six distinct polarization states. This compact mechanically tunable-free architecture enables polarization-switchable bright-field imaging, edge-enhanced imaging, and parallel imaging, offering a robust all-dielectric platform for integrated near-infrared photonics and high-fidelity polarization-multiplexed imaging systems.

The structure we propose is highly compatible with standard nanomanufacturing processes. Silicon nanopillars with a maximum aspect ratio of 4.5:1 can be fabricated. Furthermore, the single-layer architecture minimizes alignment errors, while optimized discrete phase mapping ensures high tolerance for nanoscale random size deviations. The

key to breakthroughs in future work lies in physical experimental validation. In the next step, we will comprehensively validate the actual multi-channel imaging performance of this device through systematic sample preparation, physical error assessment, and optical characterization under strictly perpendicular incident light.

Author Contributions: Writing—original draft preparation, L.Z.; writing—review and editing, W.F., S.C., M.L., X.C., X.Y., X.G. and X.F.; project administration and funding acquisition, X.F. and W.F. All authors have read and agreed to the published version of the manuscript.

Funding: This work is supported by the Cultivation Plan for Young Scholars in Universities of Shandong Province, the Natural Foundation of Shandong Province (Grant Numbers: ZR2021MF053, ZR2022MF253 and ZR2021MF070), and the Double-Hundred Talent Plan of Shandong Province, China.

Institutional Review Board Statement: Not applicable.

Informed Consent Statement: Not applicable.

Data Availability Statement: Data will be made available on request.

Conflicts of Interest: The authors declare no conflicts of interest.

References

1. Peters, C.; Forbes, A. Controlling the hidden parity in vectorial light with metasurfaces. *Adv. Photonics* **2024**, *6*, 040501. [CrossRef]
2. Yang, H.; He, H.; Hu, Y.; Duan, H. Metasurface-empowered vector light field regulation, detection and application. *Opto-Electron. Eng.* **2024**, *51*, 240168.
3. Li, M.; Li, D.; Ma, Y. Vectorial optical fields manipulation via metasurfaces. *Opto-Electron. Eng.* **2024**, *51*, 240068.
4. Pan, M.; Fu, Y.; Zheng, M.; Chen, H.; Zang, Y.; Duan, H.; Li, Q.; Qiu, M.; Hu, Y. Dielectric metalens for miniaturized imaging systems: Progress and challenges. *Light Sci. Appl.* **2022**, *11*, 195. [CrossRef] [PubMed]
5. Xiong, B.; Liu, Y.; Xu, Y.; Deng, L.; Chen, C.-W.; Wang, J.-N.; Peng, R.; Lai, Y.; Liu, Y.; Wang, M. Breaking the limitation of polarization multiplexing in optical metasurfaces with engineered noise. *Science* **2023**, *379*, 294–299. [CrossRef] [PubMed]
6. Hu, Z.; Gu, M.; Tian, Y.; Li, C.; Zhu, M.; Zhou, H.; Fang, B.; Hong, Z.; Jing, X. Review for optical metalens based on metasurfaces: Fabrication and applications. *Microsyst. Nanoeng.* **2025**, *11*, 189. [CrossRef] [PubMed]
7. Arbabi, A.; Faraon, A. Advances in optical metalenses. *Nat. Photonics* **2023**, *17*, 16–25. [CrossRef]
8. Shen, Z.; Lin, X. A review of metasurface polarization devices. *Opt. Mater.* **2023**, *146*, 114567. [CrossRef]
9. Qi, B.; Li, Y.; Chen, X. Flat Optics for Polarization Structure Engineering from 2D to 3D. *Adv. Opt. Mater.* **2025**, *13*, 2102164. [CrossRef]
10. Li, F.J.; Feng, Z.; Wan, Z.; Shi, T.; Qiu, S.; Zeng, J.-H.; Song, S.; Wang, S.; Deng, Z.-L.; Li, X. Meta-grating-lens-based monolithic polarization camera. *Sci. Adv.* **2025**, *11*, eadx9886. [CrossRef] [PubMed]
11. Yuan, S.-M.; Gao, T.; Chen, A.-L. Non-local design method of metasurface by the grating diffraction theory enabling efficient wave control. *Phys. Lett. A* **2025**, *529*, 130081. [CrossRef]
12. Wang, Q.; Li, C.; Fang, B.; Ke, L.; Lu, J.; Ma, X.; Hong, Z.; Jing, X. Flexible and independent control of asymmetric vortex beams based on spin multiplexing all dielectric metasurface. *J. Light. Technol.* **2023**, *41*, 7098–7104. [CrossRef]
13. Umar, A.A.; Zubir, F.; Yusoff, M.F.M.; Abbasi, M.I.; Shah, S.M.; Vallappil, A.K.; Assaad, M.; Jizat, N.M. Simultaneous Reflection and Transmission in Metasurfaces: A Comprehensive Review. *IEEE Access* **2026**, *14*, 46805–46829. [CrossRef]
14. Tian, S.; Han, M.; Xu, J.; Liu, H. Multifunctional Coding Metasurface for Focusing and Beam Deflection Based on Polarization Selection. *Electromagnetics* **2024**, *44*, 57–71. [CrossRef]
15. Gao, H.; Fan, X.H.; Wang, Y.X.; Liu, Y.; Wang, X.; Xu, K.; Deng, L.; Zeng, C.; Li, T.; Xia, J.; et al. Multi-foci metalens for spectra and polarization ellipticity recognition and reconstruction. *Opto-Electron. Sci.* **2023**, *2*, 220026. [CrossRef]
16. Sardana, J.; Devinder, S.; Zhu, W.; Agrawal, A.; Joseph, J. Dielectric metasurface enabled compact, single-shot digital holography for quantitative phase imaging. *Nano Lett.* **2023**, *23*, 11112–11119. [CrossRef] [PubMed]
17. Wang, J.; Yu, R.; Ye, X.; Sun, J.; Li, J.; Huang, C.; Xiao, X.; Ji, J.; Shen, W.; Tie, Z.; et al. Quantitative phase imaging with a compact meta-microscope. *npj Nanophotonics* **2024**, *1*, 4. [CrossRef]
18. Shanker, A.; Fröch, J.E.; Mukherjee, S.; Zhelyeznyakov, M.; Brunton, S.L.; Seibel, E.J.; Majumdar, A. Quantitative phase imaging endoscopy with a metalens. *Light Sci. Appl.* **2024**, *13*, 305. [CrossRef] [PubMed]
19. Zheng, C.; Li, J.; Wang, G.; Liu, J.; Yue, Z.; Zhao, H.; Hao, X.; Zhang, Y.; Zhang, Y.; Yao, J. All-dielectric metasurfaces capable of dual-channel complex amplitude modulation. *Nanophotonics* **2021**, *10*, 2959–2968. [CrossRef]

20. Zhang, Y.; Li, S.; Wu, J.; Li, Y.; Gan, F.; Zhou, W.; Zeng, Y.; He, X.; Ran, C.; Chen, J.; et al. Long-Wavelength Infrared Edge-Enhanced Imaging with a Single-Layer Silicon Vortex Metalens. *ACS Photonics* **2026**, *13*, 137–144.
21. Mu, Y.H.; Zhang, H.J.; Long, Y.; Peng, F.; Zhou, J.W. Design of Controllable Focusing Intensity Ratio Bifocal Metalens Based on Spatial Multiplexing. *Electron. Opt. Control* **2025**, *32*, 104.
22. Li, L.; Zhang, J.; Jiang, Y.T.; Pan, M.; Wang, S.; Yang, P.; Zang, Y.; Duan, H.; Hu, Y. Dielectric metalens array for simultaneous polarization and wavefront mapping in the visible spectrum. *Nano Lett.* **2025**, *25*, 10879–10887. [CrossRef] [PubMed]
23. Ji, Z.; Chen, Q.; Sha, X.; Wang, H.; Ma, X.; Liu, Z.; Song, Q.; Xiao, S. Multidimensional multiplexing metalens for STED microscopy. *Sci. Adv.* **2025**, *11*, eadt280. [CrossRef] [PubMed]
24. Jordaan, J.; Minovich, A.E.; Neshev, D.; Minovich, A.; Neshev, D.; Staude, I. Design of multilayer Huygens' metasurfaces for large-area multiwavelength and polarization-insensitive metalenses. *Opt. Express* **2025**, *33*, 33643–33654. [CrossRef] [PubMed]
25. Brongersma, M.L.; Pala, R.A.; Altug, H.; Capasso, F.; Chen, W.T.; Majumdar, A.; Atwater, H.A. The second optical metasurface revolution: Moving from science to technology. *Nat. Rev. Electr. Eng.* **2025**, *2*, 125–143. [CrossRef]
26. Wang, W.; Zhao, R.; Kang, Q.; Wang, R.; Liu, X.; Liu, T.; Fan, S.-W.; Guo, Z. Photonic spin Hall effect driven broadband multi-focus dielectric metalens. *Appl. Opt.* **2023**, *62*, 8159–8167. [CrossRef] [PubMed]
27. Ma, L.F.; Wu, Y.; Xie, B.; Wang, J.; Chang, J.; Jiang, H. Research on Infrared Polarizing Elements and Optical Systems Based on Metasurface. *Proc. SPIE* **2024**, *13236*, 132360U.
28. Zhou, C.; Zheng, Y.; He, G.; Li, S.; Deng, Y.; Zhang, H.; Zhou, Z.-K. Generating arrays of perfect vector vortex beam with six on-demand degrees of freedom in metasurfaces. *Sci. China Phys. Mech. Astron.* **2025**, *68*, 254211. [CrossRef]
29. Zhao, F.X.; Dong, P.; Zhang, M. Single-layer terahertz metasurface for multichannel vortex device based on polarization multiplexing. *Proc. SPIE* **2024**, *13244*, 132440U.
30. Swartz, B.T.; Zheng, H.; Forcherio, G.T.; Valentine, J. Broadband and large-aperture metasurface edge encoders for all-optical edge detection. *Sci. Adv.* **2024**, *10*, eadk0024. [CrossRef] [PubMed]
31. Shan, X.; Li, Z.; Li, J.; Li, Z.; Li, J.; Fu, R.; Zhou, Z.; He, Z.; Zheng, G. Broadband continuous achromatic and super-dispersive metalens in near-infrared band. *J. Appl. Phys.* **2022**, *131*, 023103. [CrossRef]
32. Liu, T.; Dai, C.; Wang, D.; Chan, C.T.; Zhou, L. High-efficiency vectorial holography based on ultra-thin metasurfaces. *Adv. Photonics* **2025**, *7*, 056004. [CrossRef]
33. Feng, K.; Feng, H.; Gu, M.; Li, C.; Jing, X. Generation and Manipulation of Perfect Vortex Beams via Metasurfaces. *Ann. Phys.* **2025**, *538*, 2500426. [CrossRef]
34. Sun, X.; He, J.; Yan, Z.; Wang, Y.; Tao, H.; Yang, X.; Wang, J. Generation and control of high-reflection-efficiency perfect vortex beams based on all-dielectric metasurfaces. *Chin. Opt. Lett.* **2025**, *23*, 281432671. [CrossRef]
35. He, X.; Wu, M.; Lu, G.; Zhang, Y.; Geng, Z. High-efficiency multi-channel focusing and imaging enabled by polarization-frequency multiplexing non-interleaved metasurfaces. *Photonics Res.* **2025**, *13*, 976. [CrossRef]
36. Jin, X.; He, Y.; Li, J.; Nie, X.; Du, S.; Song, Y.; Luo, H.; Liu, M.; Ma, S.; He, Q.; et al. Generating vectorial optical fields via surface-wave-excited complex-amplitude metasurfaces. *Light Sci. Appl.* **2026**, *15*, 256. [CrossRef] [PubMed]
37. Jiang, H.X.; Sheng, L.; Luo, Y.; Meng, L.; Cao, W. Design of Tunable Broadband Graphene-Based Metasurface with Amplitude-Phase Modulation. *Materials* **2023**, *16*, 4633. [CrossRef] [PubMed]
38. Wang, X.; Xu, K.; Fan, X.; Liu, Y.; Yu, X.; Gao, H.; Xiong, W. Transversely Dispersive Multi-Foci Metalens Based on Selective Spectral Response Structure. *Chin. J. Lasers* **2023**, *50*, 1813014.
39. Li, C.; Liu, C.; Peters, C.; Yu, H.; Maier, S.A.; Forbes, A.; Ren, H. Disordered mosaic metasurfaces with scalable functional density. *Nat. Commun.* **2026**, *17*, 4835. [CrossRef] [PubMed]
40. Chen, X.; Zhang, Y.; Zeng, Y.; Deng, Y.; Zhao, F.; Zhou, W.; Li, Y.; Yuan, M.; Tong, K.; Fan, L.; et al. Multifunctional LWIR metalens integrating polarimetric detection, bright-field imaging, and edge enhancement. *Opt. Express* **2026**, *34*, 15905. [CrossRef] [PubMed]
41. Yao, J.; Fan, Y.; Gao, Y.; Lin, R.; Wang, Z.; Chen, M.K.; Xiao, S.; Tsai, D.P. Nonlocal Huygens' meta-lens for high-quality-factor spin-multiplexing imaging. *Light Sci. Appl.* **2025**, *14*, 65. [CrossRef] [PubMed]
42. Wu, S.; Wang, W.; Li, G.; Ji, T.; Hao, Y.; Cui, Y.; Nie, Z. 4H-SiC-based polarization-multiplexed metalens balancing high NA and focusing efficiency in near-infrared bands. *Opt. Lett.* **2025**, *50*, 5474. [CrossRef] [PubMed]
43. Khalilian, A.; Yu, B.; Tsoi, K.; Yi, Y. High-numerical-aperture and high-efficiency polarization-based metalenses with pitch size control utilizing silicon-rich nitride. *Opt. Lett.* **2025**, *50*, 503. [CrossRef] [PubMed]

Disclaimer/Publisher's Note: The statements, opinions and data contained in all publications are solely those of the individual author(s) and contributor(s) and not of MDPI and/or the editor(s). MDPI and/or the editor(s) disclaim responsibility for any injury to people or property resulting from any ideas, methods, instructions or products referred to in the content.